Petroleum Science 22 (2025) 4573–4583

Contents lists available at ScienceDirect

Petroleum Science

journal homepage: www.keaipublishing.com/en/journals/petroleum-science

Original Paper

Joint PP and PS seismic inversion using predicted PS waves from deep learning

Xin Fu [a], Feng Zhang [b,*], Dan-Ping Cao [a]

[a] State Key Laboratory of Deep Oil and Gas, China University of Petroleum (East China), Qingdao, 266580, Shangdong, China
[b] College of Geophysics, China University of Petroleum (Beijing), Beijing, 102249, China

ARTICLE INFO

Article history:
Received 6 June 2024
Received in revised form
18 June 2025
Accepted 2 August 2025
Available online 9 August 2025

Edited by Meng-Jiao Zhou

Keywords:
Joint inversion
Deep learning
PP waves
cGAN
Shear wave prediction

ABSTRACT

Seismic AVO/AVA (amplitude-versus-offset or amplitude-versus-angle) analysis, based on prestack seismic angle gathers and the Zoeppritz equation, has been widely used in seismic exploration. However, conducting the multi-parameter AVO/AVA inversion using only PP-wave angle gathers is often highly ill-posed, leading to instability and inaccuracy in the inverted elastic parameters (e.g., P- and S-wave velocities and bulk density). Seismic AVO/AVA analysis simultaneously using both PP-wave (pressure wave down, pressure wave up) and PS-wave (pressure wave down, converted shear wave up) angle gathers has proven to be an effective method for reducing reservoir interpretation ambiguity associated with using the single wave mode of PP-waves. To avoid the complex PS-wave processing, and the risks associated with PP and PS waveform alignment, we developed a method that predicts PS-wave angle gathers from PP-wave angle gathers using a deep learning algorithm—specifically, the cGAN deep learning algorithm. Our deep learning model is trained with synthetic data, demonstrating a strong fit between the predicted PS-waves and real PS-waves in a test datasets. Subsequently, the trained deep learning model is applied to actual field PP-waves, maintaining robust performance. In the field data test, the predicted PS-wave angle gather at the well location closely aligns with the synthetic PS-wave angle gather generated using reference well logs. Finally, the P- and S-wave velocities estimated from the joint PP and PS AVA inversion, based on field PP-waves and the predicted PS-waves, display a superior model fit compared to those obtained solely from the PP-wave AVA inversion using field PP-waves. Our contribution lies in firstly carrying out the joint PP and PS inversion using predicted PS waves rather than the field PS waves, which break the limit of acquiring PS-wave angle gathers.

1. Introduction

Seismic AVO/AVA (amplitude-versus-offset or amplitude-versus-angle) analysis, based on prestack seismic angle gathers and the Zoeppritz equation (Zoeppritz, 1919), has been widely used. It is commonly employed to invert isotropic elastic parameters and, if conditions permit, can also be used to invert anisotropic parameters (Fu et al., 2018; Zhang et al., 2019; Fu, 2024). It plays a crucial role in prestack seismic inversions, representing a widely adopted approach for extracting elastic property information from seismic data. This information holds considerable importance in hydrocarbon exploration, aiding in reservoir prediction, lithological identification, and structural analysis (Liu et al., 2019; Wu et al., 2023a, 2023b). However, conducting the multi-parameter AVO/AVA inversion using only PP-wave angle gathers is often highly ill-posed, leading to instability and inaccuracy in the inverted elastic parameters (e.g., P- and S-wave velocities and bulk density).

Seismic AVO/AVA analysis using both PP-wave (pressure wave down, pressure wave up) and PS-wave (pressure wave down, converted shear wave up) angle gathers has proven to be an effective method for reducing reservoir interpretation ambiguity associated with using the single wave mode of PP-waves. Simultaneously utilizing PP-wave and PS-wave seismic data to estimate rock and fluid properties contributes to a more comprehensive understanding of subsurface geology and fluid content. Compared with PP-wave AVO/AVA inversion, joint PP and PS AVO/AVA

* Corresponding author.
E-mail address: zhangfeng@cup.edu.cn (F. Zhang).
Peer review under the responsibility of China University of Petroleum (Beijing).

https://doi.org/10.1016/j.petsci.2025.08.003

inversion can provide more accurate estimates of elastic parameters. Nevertheless, the hindrances of using PS waves are pronounced. Firstly, obtaining PS waves requires conducting a multi-component (3C) seismic survey, which is much more expensive than a single-component seismic survey. Secondly, PS-wave processing is more complicated compared to PP-wave processing, given that the propagation ray paths of PS waves are asymmetrical. Thirdly, since travel times between PP and PS waves are different, aligning PP- and PS-waves is challenging, typically requiring distorting the wavelets and knowing internal P-wave to S-wave velocity ratios a priori. To avoid complicated PS-wave processing, and the risky alignment of PP and PS waveform, we develop a method to predict PS-wave angle gathers from PP-wave angle gathers using a deep learning algorithm in this study. Then the predicted PS-wave angle gathers are employed to conduct the joint PP and PS inversion.

Deep learning algorithms, which are extensions of machine learning, have found widespread applications in various aspects of seismic studies. This study contributes to this expanding field by leveraging deep learning algorithms to predict PS-wave angle gathers, introducing a novel seismic application for these algorithms. More specifically, we employ a conditional generative adversarial network (cGAN) called Pix2Pix (Isola et al., 2017) to predict PS-wave angle gathers from the corresponding PP-wave angle gathers. GANs (Goodfellow et al., 2014) consist of two neural networks—a generator and a discriminator—trained adversarially to generate realistic data samples. In seismic processing, GANs can be applied to reconstruct missing data (Oliveira et al., 2018; Wei et al., 2021; Fu et al., 2025), build velocity models (Yang and Ma, 2019; Zhang et al., 2019), and so on. The cGAN (Mirza and Osindero, 2014) is a type of machine learning model that combines the principles of generative adversarial networks (GANs) with conditional input information. In a cGAN, both the generator and discriminator are conditioned on additional information, such as labels, guiding the learning process. Pix2Pix, a specific implementation of the cGAN, is a general deep learning framework designed to solve problems posed as image-to-image translation, i.e., mapping from input images to output images, such as translating sketches or abstract depictions into more refined and realistic images (Isola et al., 2017). Predicting PS-wave angle gathers from PP-wave angle gathers can also be turned into an image-to-image translation problem, motivating us to use Pix2Pix to carry it out.

The remaining content of this paper is organized as follows: In the Methodology section, we briefly introduce the cGAN algorithm. Next, in the Experiments section, we train and test the cGAN. Subsequently, in the Field data application section the trained deep learning model is applied to a field PP-wave datasets and the predicted PS-waves are used to conduct joint PP and PS inversion. Finally, we conclude the entire study in the Conclusion section.

2. Methodology

2.1. Fracture parameters and a new fracture gas indication factor

First introduced by Goodfellow et al. (2014), GANs have gained widespread adoption within the computer vision community over the past ten years. Comprising a generator (G) responsible for generating synthesized images ($G(x)$) and a discriminator (D) tasked with distinguishing between synthesized and real images, GANs operate through an adversarial training scheme. This scheme involves the generator (G) learning to produce realistic images from random noise vectors to deceive the discriminator (D), while the discriminator endeavors to accurately discriminate between synthesized and real images.

In contrast to GANs, the cGAN based on Pix2Pix learns a mapping from the input image x to the target image y, and y is used to condition the GAN. The sketch of cGAN used in our study is plotted in Fig. 1, where the inputs (x) are PP-wave angle gathers, the target outputs (y) are PS-wave angle gathers, and both G and D are conditioned on PS-wave angle gathers. The goal is still to train a G generating y that cannot be discriminated by D and train a D that can discriminate the y obtained from G.

The loss function for a cGAN without a random noise vector as input can be formulated as (Mirza and Osindero, 2014; Isola et al., 2017):

$$L_{\mathrm{cGAN}}(G,D) = E_{x,y}[\log D(x,y)] + E_x[\log(1 - D(x,G(x)))] \tag{1}$$

where G aims to minimize this objective in contrast to an adversarial D, which endeavors to maximize it, i.e.,

$$G^* = \arg\min_G \max_D L_{\mathrm{cGAN}}(G,D) \tag{2}$$

G^* is the solution that minimizes the generator's loss against the maximally adversarial discriminator D in the context of the cGAN with respect to the loss function $L_{\mathrm{cGAN}}(G, D)$. Earlier methods (Pathak et al., 2016) have discovered advantages in combining the GAN objective with a conventional loss, such as L_2 distance, and Isola et al. (2017) illustrate that the utilization of L_1 distance, as opposed to L_2, is conducive to minimizing blurring effects. The L_1 distance is:

$$L_{\mathrm{L1}}(G) = E_{x,y}[\|y - G(x)\|_1] \tag{3}$$

Thus, the final cGAN objective function applied in Pix2Pix is:

$$G^* = \arg\min_G \max_D L_{\mathrm{cGAN}}(G,D) + \lambda L_{\mathrm{L1}}(G) \tag{4}$$

where G^* is the solution that minimizes the combined loss of the cGAN ($L_{\mathrm{cGAN}}(G, D)$) and the L_1 loss ($L_{\mathrm{L1}}(G)$), with λ as a hyper-parameter controlling the trade-off between the two terms.

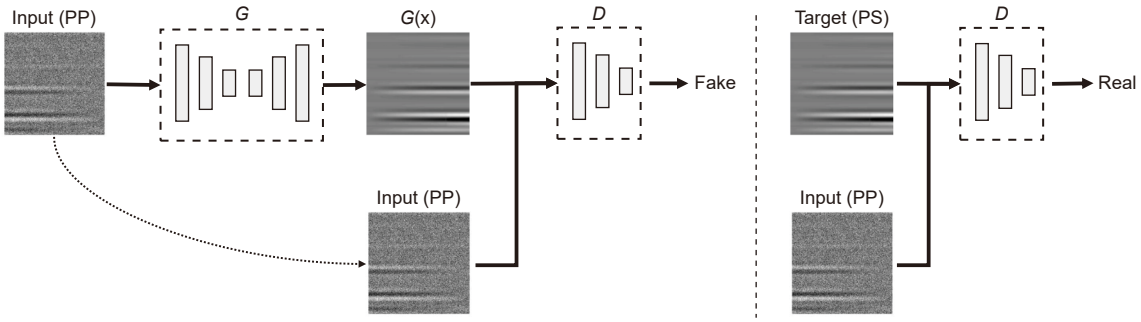

Fig. 1. Workflow for cGAN. The inputs are PP-wave angle gathers and the target outputs are PS-wave angle gathers.

In Pix2Pix (Isola et al., 2017), the generator and discriminator are "Unet" and "PatchGAN", respectively, distinguishing it from other GANs. This design adheres to a U-Net fully convolutional neural network structure (Ronneberger et al., 2015), consisting of a series of encoder blocks succeeded by a series of decoder blocks. The inclusion of skip connections strengthens pattern recognition at various scales. The discriminator adopts a "PatchGAN" architecture (Ioffe and Szegedy, 2015; Radford et al., 2015), incorporating a series of encoder blocks culminating in a concise data representation. Each pixel in this representation encodes the probability of the associated patch belonging to a real-data distribution. Both the generator and discriminator employ encoder blocks following the structure of Convolution-BatchNorm-ReLu, while the decoders in the generator adhere to the pattern of Deconvolution-BatchNorm-ReLu (Ioffe and Szegedy, 2015; Isola et al., 2017; Oliveira et al., 2018).

3. Experiments

3.1. Training and test data

The training and testing data used in this study are synthesized data based on the Zoeppritz equation. At the interface of two subsurface rock layers, when a downward P-wave encounters it, it generates reflections of upward P-wave and converted S-wave, i.e., PP-wave and PS-wave. The corresponding reflection coefficients in isotropic media can be expressed exactly using the Zoeppritz equation. Accurate solutions to the Zoeppritz equation for PP and PS-wave reflection coefficients are provided by (Aki and Richards, 2002)

$$R_{PP}(\theta_1) = \left[\left(B\frac{\cos\theta_1}{\alpha_1} - C\frac{\cos\theta_2}{\alpha_2}\right)F - \left(A + D\frac{\cos\theta_1}{\alpha_1}\frac{\cos\varphi_2}{\beta_2}\right)Hp^2\right] \Big/ I \tag{5}$$

and

$$R_{PS}(\theta_1) = -2\frac{\cos\theta_1}{\alpha_1}\left(AB + CD\frac{\cos\theta_2}{\alpha_2}\frac{\cos\varphi_2}{\beta_2}\right)p\alpha_1 \Big/ (\beta_1 I) \tag{6}$$

where

$$\begin{cases} A = \rho_2\left(1 - 2\beta_2^2p^2\right) - \rho_1\left(1 - 2\beta_1^2p^2\right) \\ B = \rho_2\left(1 - 2\beta_2^2p^2\right) + 2\rho_1\beta_1^2p^2 \\ C = \rho_1\left(1 - 2\beta_1^2p^2\right) + 2\rho_2\beta_2^2p^2 \\ D = 2\left(\rho_2\beta_2^2 - \rho_1\beta_1^2\right) \end{cases} \tag{7}$$

$$\begin{cases} E = B\frac{\cos\theta_1}{\alpha_1} + C\frac{\cos\theta_2}{\alpha_2}, \\ F = B\frac{\cos\varphi_1}{\beta_1} + C\frac{\cos\varphi_2}{\beta_2}, \\ G = A - D\frac{\cos\theta_1}{\alpha_1}\frac{\cos\varphi_2}{\beta_2}, \\ H = A - D\frac{\cos\theta_2}{\alpha_2}\frac{\cos\varphi_1}{\beta_1}, \\ I = EF + GHp^2 \end{cases} \tag{8}$$

and

$$\begin{cases} p = \frac{\sin\theta_1}{\alpha_1}, \\ \theta_2 = \sin^{-1}\left(\frac{\alpha_2}{\alpha_1}\sin\theta_1\right), \\ \varphi_1 = \sin^{-1}\left(\frac{\beta_1}{\alpha_1}\sin\theta_1\right), \\ \varphi_2 = \sin^{-1}\left(\frac{\beta_2}{\alpha_1}\sin\theta_1\right), \end{cases} \tag{9}$$

The PP-wave and PS-wave coefficients are expressed in terms of the P-wave incident angle θ_1 as well as P wave velocities (α_1, α_2), S-wave velocities(β_1, β_2), and densities(ρ_1, ρ_2) of the upper and lower rock layers at the interface.

Based on Eq. (5) and Eq. (6), we generated 1000 input-target image pairs as training data and 100 input-target image pairs as test data, four of which are plotted in Fig. 2. In each pair, the left half is the target image, i.e., the PS-wave angle gather at a certain location, and the right half is the corresponding input image, i.e., the PP-wave angle gather. For both PP and PS-wave angle gathers, the horizontal axis represents the P-wave incident angle in a range of [0°, 35°], and the vertical axis represents the travel time. The image size for both PP- and PS-waves is identical, at 256 × 256.

The steps for generating a single input-target image pair are outlined below and illustrated in Fig. 3:

(1) To obtain a segment of the P-wave velocity model, a random and vertical selection of a trace from the Marmosusi model (Versteeg, 1994) is made, and a 1D nearest-neighbor interpolation is then applied to extend it to a length of 257 (one more than the image vertical pixel number).
(2) Use Gardner's equation $\rho = a\alpha^b$ (Gardner et al., 1974) and the P-and S-wave empirical relation $\beta = (\alpha - c)/d$ (Castagna et al., 1985) to calculate S-wave velocity (β) and density (ρ) from P-wave velocity (α). Here, a, b, c, and d are randomly selected from the ranges [1.3, 1.8], [0.1, 0.4], [0.9, 1.4], and [0.9, 1.5], respectively. The empirical equations and ranges employed here aim to ensure that the generated training and test data possess both physical relevance and broad applicability simultaneously.
(3) Use Eq. (5) and Eq. (6) to calculate reflectivities for P-wave incident angles varying in the range of [0°, 35°].
(4) Generate a Ricker wavelet with a randomly chosen dominant frequency from the range of [20, 50] Hz, and the time sampling rate is identical to that of the models obtained above.
(5) Convolve the wavelet with the reflectivities to obtain synthetic PP- and PS-wave angle gathers, and they have the same wavelet.
(6) Add Gaussian noise to the PP-wave angle gather, and the SNR (signal to-noise ratio) is randomly chosen in the range of [0, 10] dB.
(7) Convert PP (input) and PS (target) data to grayscale images. We use a U-Net architecture, which requires input data in a consistent 2D image format. To ensure compatibility, we reshape the seismic angle gathers into a fixed 256 × 256 size. The original angle gathers (e.g., 256 × 35) are padded or interpolated to match the required dimensions while preserving key features. This allows the network to fully leverage its convolutional structure for effective feature extraction and prediction.

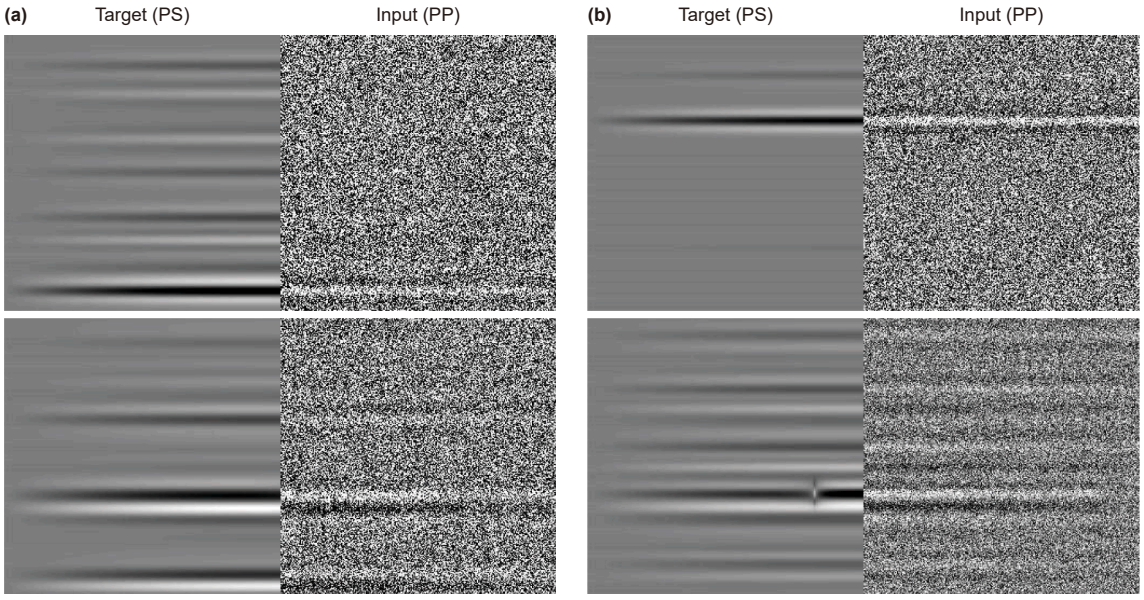

Fig. 2. Four image pairs out of the 1000 image pairs used as training data are presented. In **(a)** and **(b)**, the left image is the target, representing a noise-free PS-wave angle gather, and the right image is the input, depicting a noisy PP-wave angle gather. In each image of each panel, the horizontal axis represents the incident angle, ranging from 1° to 35°, while the vertical axis represents the time index, ranging from 1° to 256°.

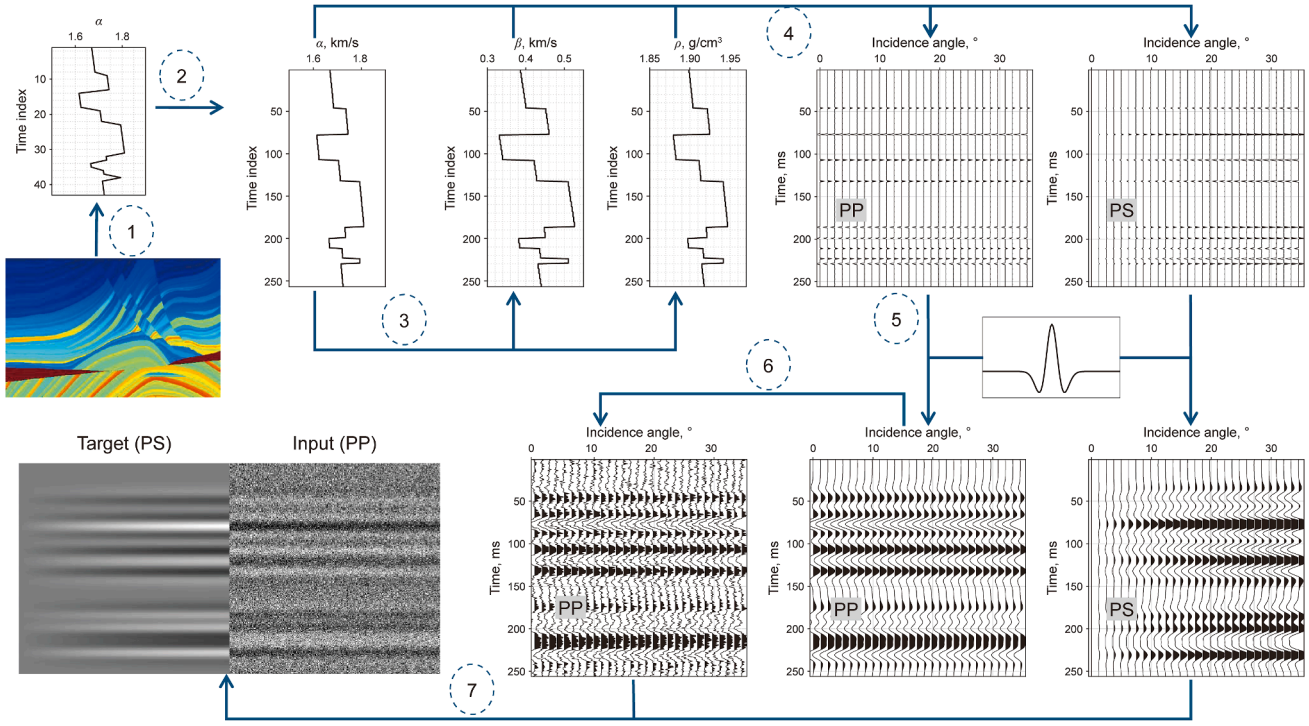

Fig. 3. Workflow for generating training data. Each input-target image pair is created through the following steps: (1) Randomly select a segment of the P-wave velocity (α) trace from the 2D Marmousi model. (2) Extend the selected P-wave velocity trace to a length of 257. (3) Calculate the S-wave velocity (β) and density (ρ) using empirical equations with randomly assigned parameters. (4) Compute the PP- and PS-wave reflection coefficients using Eq. (5) and Eq. (6). (5) Convolve the reflection coeffcients with a wavelet of random dominant frequency. (6) Add random noise to PP waves. (7) Convert PP (input) and PS (target) data to gray scale images.

In the training data generation process, to improve the diversity and representativeness of the training datasets, we generated input-output pairs by introducing multiple sets of random perturbations into the forward modeling process, which was based on the Zoeppritz equations and convolution. The P-wave velocity model was constructed by randomly selecting segments from the Marmousi model and extending them to predefined lengths, introducing variability in both the number of subsurface layers and their physical properties. The corresponding S-wave velocity and density models were derived from the P-wave model using empirical relationships, with additional random perturbations applied to the formula parameters to further enhance variability.

To simulate the stochastic noise commonly present in real seismic data, Gaussian white noise with varying signal-to-noise ratios was added.

3.2. Training scheme and results

We do not tune the training parameters, and all training processes are identical to those in Isola et al. (2017), as the same parameters have already provided satisfactory results. The training encompasses 80,000 epochs, where each epoch involves 1000 training image pairs and 100 test image pairs. We employ the Adam optimizer with an initial learning rate of 0.0002 and a momentum of 0.5, and the batch size is set to 1. The loss functions for the generator and discriminator are both the sigmoid cross-entropy loss. The weight parameter (λ) for the L_1 generator loss function is set to 100.

Some of the predicted results using the test PP-wave angle gathers that are not used for training are plotted in Fig. 4, and some traces are extracted and plotted in Fig. 5. A noise-free PP-wave event should be flat. However, during training, we added noise to make the PP-wave event non-flat, which better reflects real-world conditions. When predicting PS-waves from PP-waves, we also take into account the denoising capability of the deep learning model, so the predicted PS-waves are noise-free and flat. We observe the predicted PS-wave angle gathers using noisy PP-waves can well fit the real PS-wave angle gathers. This demonstrates the success of our model training, and the trained model will be adopted to predict PS-waves using field PP-wave angle gathers in the next section to further demonstrate the generalization of the model in practice.

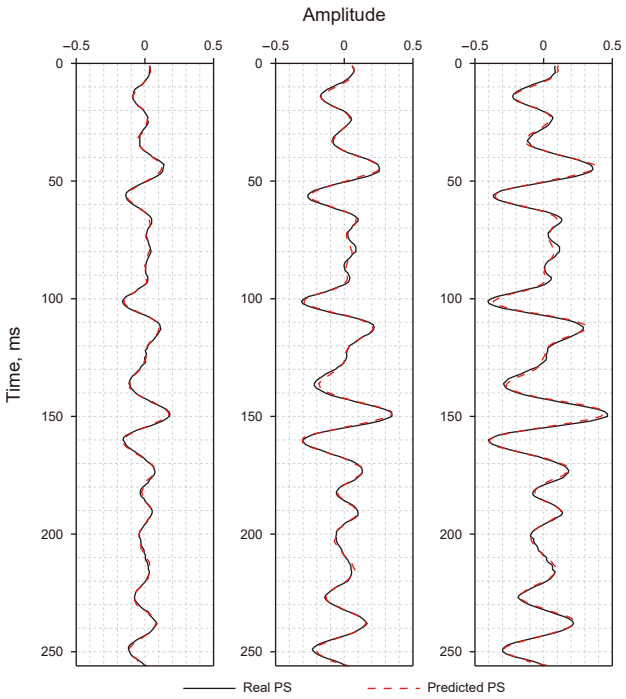

Fig. 5. Traces randomly extracted from a certain test result. The solid black curves are from a noise-free real PS-wave angle gather, and the dashed red curves are from the corresponding predicted PS-wave angle gather.

4. Field data application

In this section, a field datasets of PP-wave angle gathers is utilized to further test the trained deep learning model. Initially, we employ the model trained on the synthetic datasets from the previous section to predict PS-wave angle gathers from the field PP-wave data. Subsequently, we utilize both the field PP-waves and the predicted PS-waves to conduct the joint PP and PS AVA inversion. Additionally, well log data is employed to illustrate the effectiveness of using the predicted PS waves.

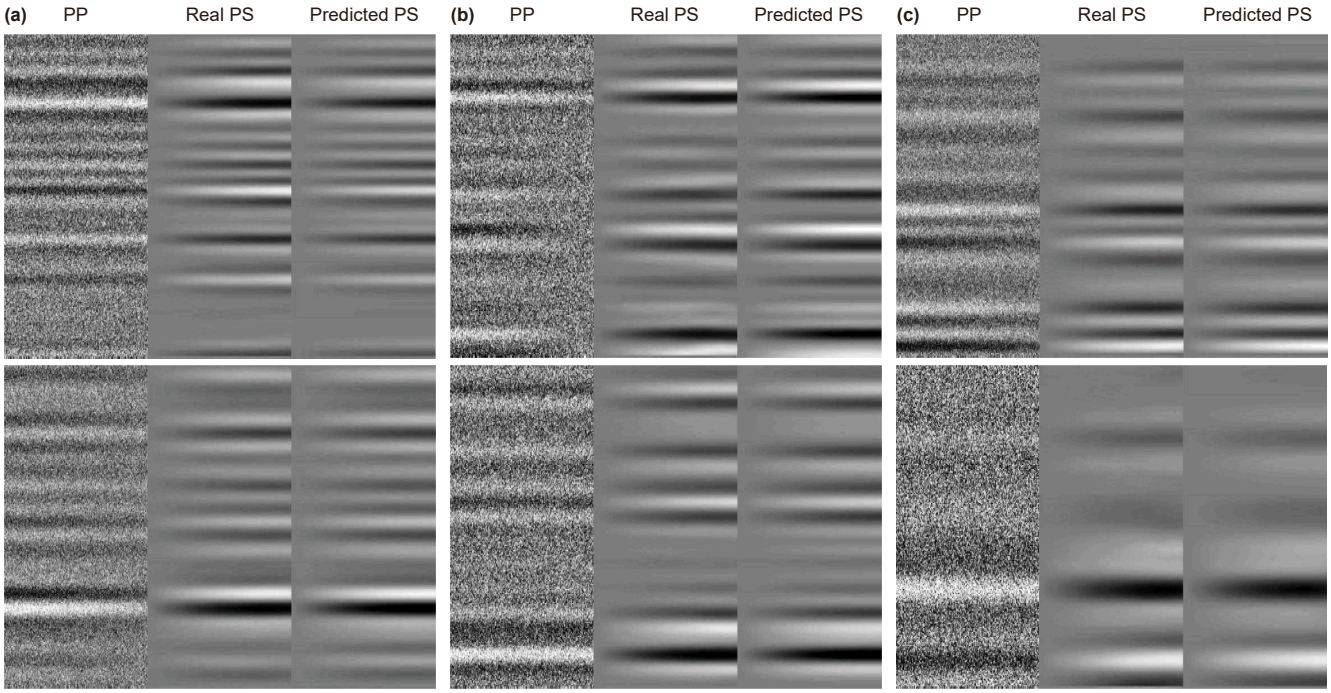

Fig. 4. Six image pairs are randomly selected from the 100 image pairs of tested results. In **(a)**, **(b)** and **(c)**, the left image is the input, depicting a noisy PP-wave angle gather; the middle image is the target, representing the corresponding noise-free real PS-wave angle gather, and the right image is the output of the trained generator, denoting the predicted PS-wave angle gather.

4.1. Joint PP and PS inversion

Normally, the objective function of PP and PS joint AVA inversion is given by the following least-squares misfit function:

$$E(m) = \frac{1}{2}(1-\mu_1)\|D_{PP} - W_{PP}*R_{PP}\|_2^2 + \frac{\mu_1}{2}\|D_{PS} - W_{PS}*R_{PS}\|_2^2 + \frac{1}{2}\mu_2 m^T C_m^{-1} m \tag{10}$$

where the first term represents the misfit of PP-wave data, the second term is the misfit of PS-wave data, and the third term is the regularization term. D_{PP} is the field PP-wave angle gather data vector, and D_{PS} is the PS-wave angle gather data vector, which is predicted in this study. R_{PP} and R_{PS} are synthetic PP- and PS-wave angle gather data vectors, respectively, depending on the subsurface model parameter vector m and calculated from Eq. (5) and Eq. (6). W_{PP} and W_{PS} are, respectively, PP- and PS-wave wavelet matrices. C_m is the model covariant matrix. μ_1 is the trade of parameter between PP- and PS-wave data, and μ_2 is the trade of parameter between data misfit and the regularization term. In this study, μ_1 is set to 0.5 for joint PP and PS inversion and 0 for PP-wave inversion, while μ_2 is adjusted accordingly. The objective function is solved by the Gaussian Newton algorithm.

To demonstrate the qualification of the inversion program, we utilize noise-free and noisy (SNR = 0.2 dB) synthetic PP- and PS-waves to conduct PP-wave inversion and joint PP and PS inversion. The inverted results are respectively plotted in Figs. 6 and 7, where we observe that PP-wave inversion and joint inversion exhibit similar performance when the data is noise-free, and the joint inversion performs better when the data are noisy. Note that some of the discrepancy between the true and inverted values results from the band-limited nature of seismic data, which restricts the resolution of high-frequency details and leads to mismatches with the true curve.

4.2. Field data inversion

The field PP-wave data come from the western Sichuan Basin in southwestern China. The incident angles are in the range of [0°, 35°], identical to that used to train the deep learning model. The partial stacking PP-wave seismic sections are plotted in Fig. 8, and the partial stacking predicted PS-waves are plotted in Fig. 9. The PS-wave seismic exhibits the same geological structure as the PP-waves, and their amplitude polarities are opposite to each other. The estimated wavelets of the partial stacking PP and PS seismic sections are plotted in Fig. 10. Theoretically, the PP- and PS-waves should have identical wavelets, but the estimated PP-wave wavelets are hard to be accurate; therefore, a safer way is to estimate PP- and PS-wave wavelets separately.

To observe the performance of the trained model intuitively, we use the well logs at CDP 1396 to generate synthetic PP- and PS-waves, plotted in Fig. 10(a) and (b). For comparison, the field PP-wave angle gather at the well location is plotted in Fig. 10(c), and the corresponding predicted PS-wave angle gather is plotted in Fig. 10(d). We observe that the field PP-waves are well tied to the well logs, and the predicted PS-waves are similar to the synthetic PS-waves from well logs.

The initial P- and S-wave velocity models and the inverted P- and S-wave velocity results of the PP-wave inversion and the joint PP and PS inversion are plotted in Fig. 11, with their traces at the well location shown in Fig. 12, where the well logs are also plotted as references. We observe that the joint inversion results better fit

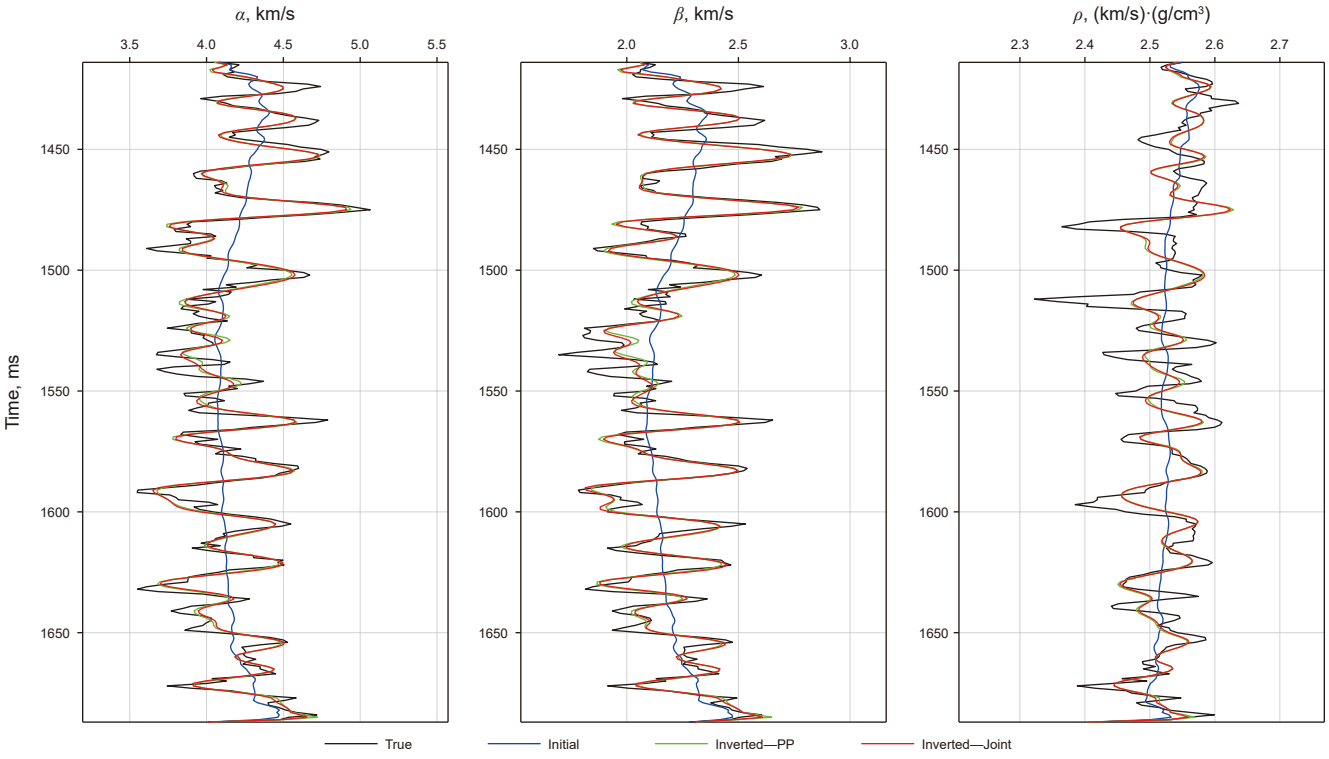

Fig. 6. Inverted results using noise-free synthetic data. The black curves represent the true values of model parameters, the blue curves represent the initial model, the green curves represent the inverted values of the PP-wave inversion, and the red curves represent the inverted values of the joint PP and PS inversion. α, β, and ρ represent the P-wave velocity, S-wave velocity, and density, respectively.

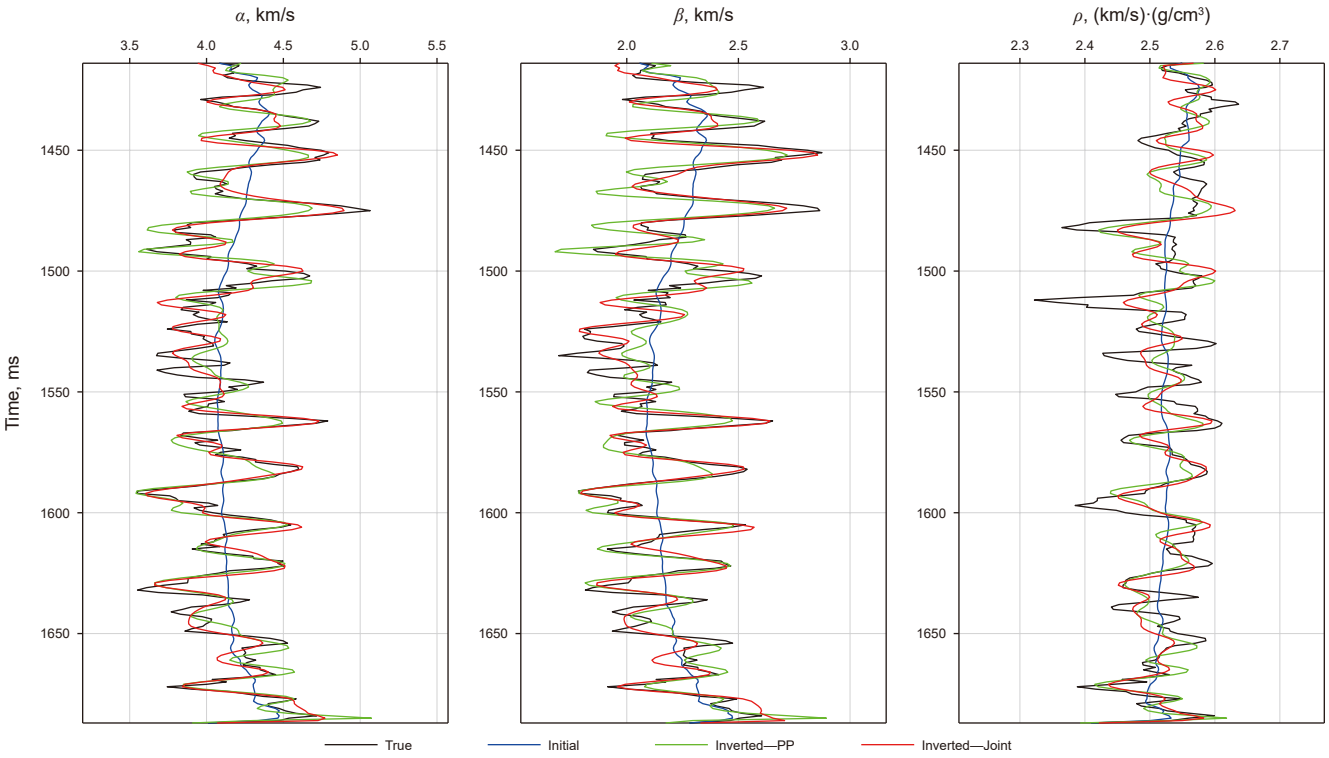

Fig. 7. Inverted results using noisy synthetic data. The black curves represent the true values of model parameters, the blue curves represent the initial model, the green curves represent the inverted values of the PP-wave inversion, and the red curves represent the inverted values of the joint PP and PS inversion. α, β, and ρ represent the P-wave velocity, S-wave velocity, and density, respectively.

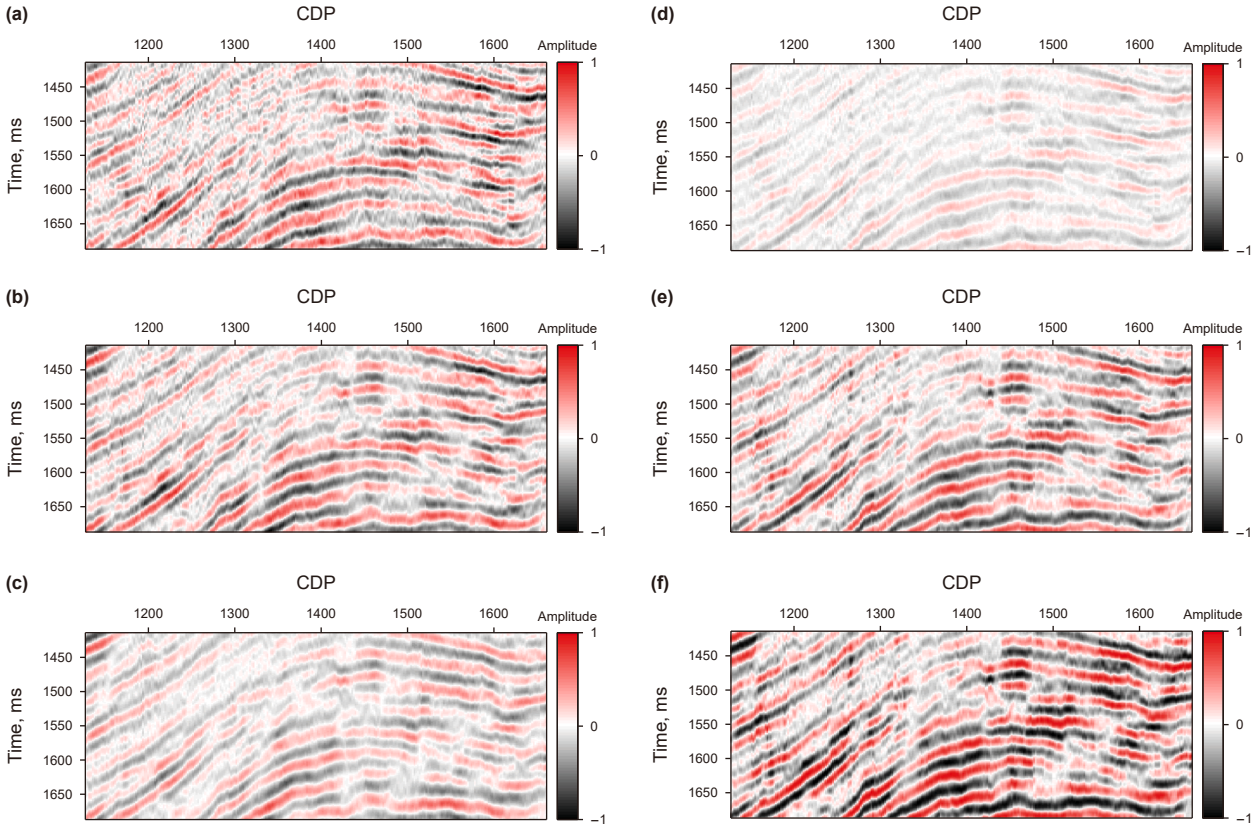

Fig. 8. Field PP-wave and predicted PS-wave partial stacking seismic sections. Panels **(a)**, **(b)**, and **(c)** represent PP-wave near-, middle-, and far-offset stacking seismic sections, respectively. Panels **(d)**, **(e)**, and **(f)** represent PS-wave near-, middle-, and far-offset stacking seismic sections, respectively.

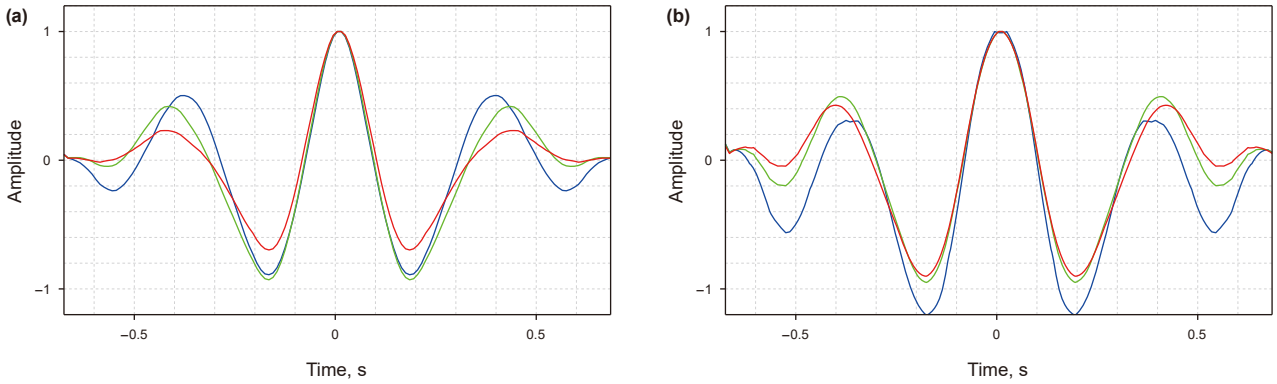

Fig. 9. Estimated wavelets of the partial stacking seismic sections in Fig. 8. Wavelets in panel **(a)** are for PP-waves, and those in panel **(b)** are for PS-waves. The blue, green, and red curves correspond to the near-, middle-, and far-offset partial stacking seismic sections, respectively.

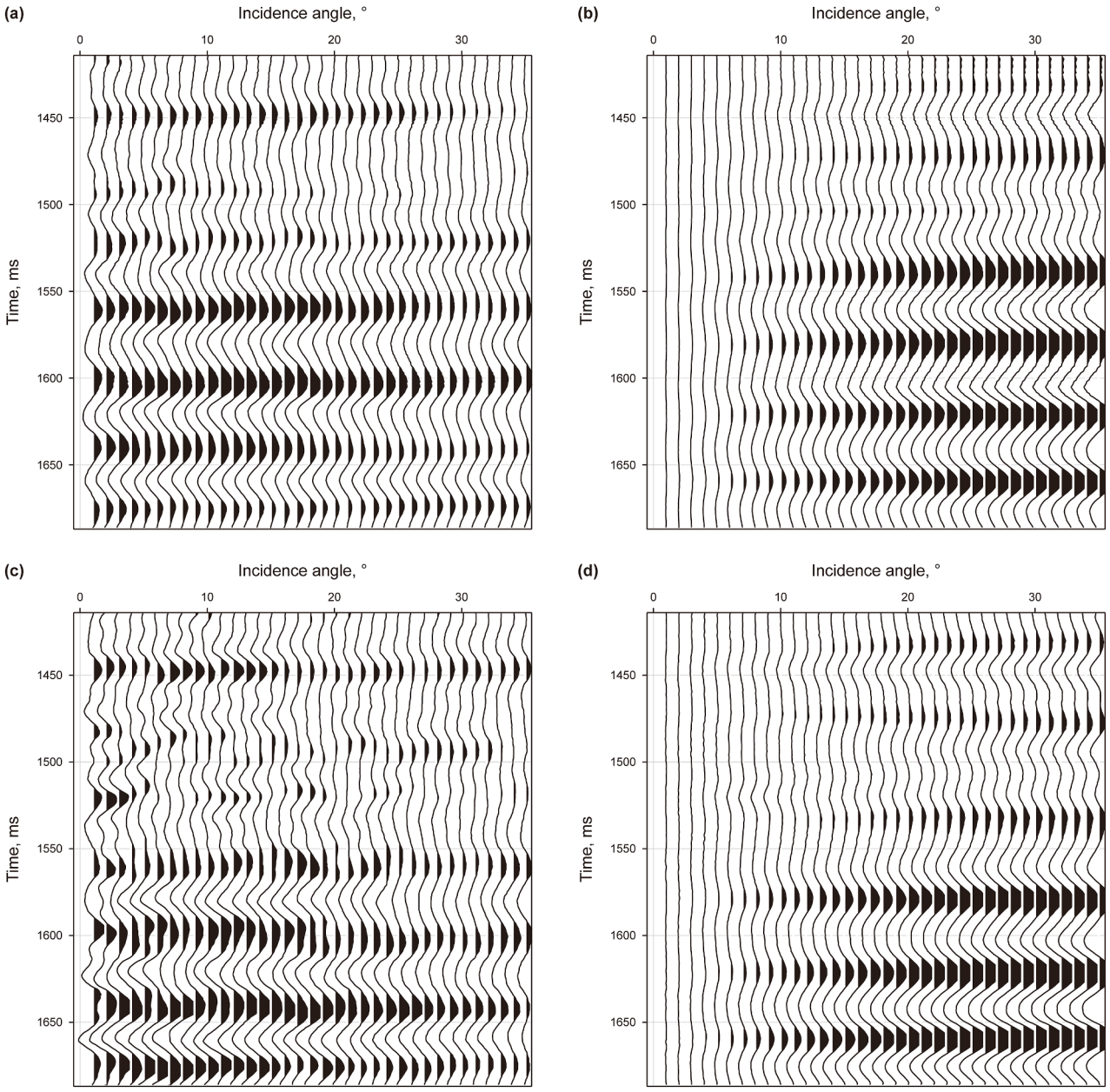

Fig. 10. Panels **(a)** and **(b)**, respectively, represent the synthetic PP- and PS-wave angle gathers generated using well-log data. Panels **(c)** and **(d)**, respectively, represent field PP-wave and predicted PS-wave angle gathers at the well location. The wavelets used to generate the synthetic data vary with the incident angle, which is more realistic than applying a single constant wavelet across all angles.

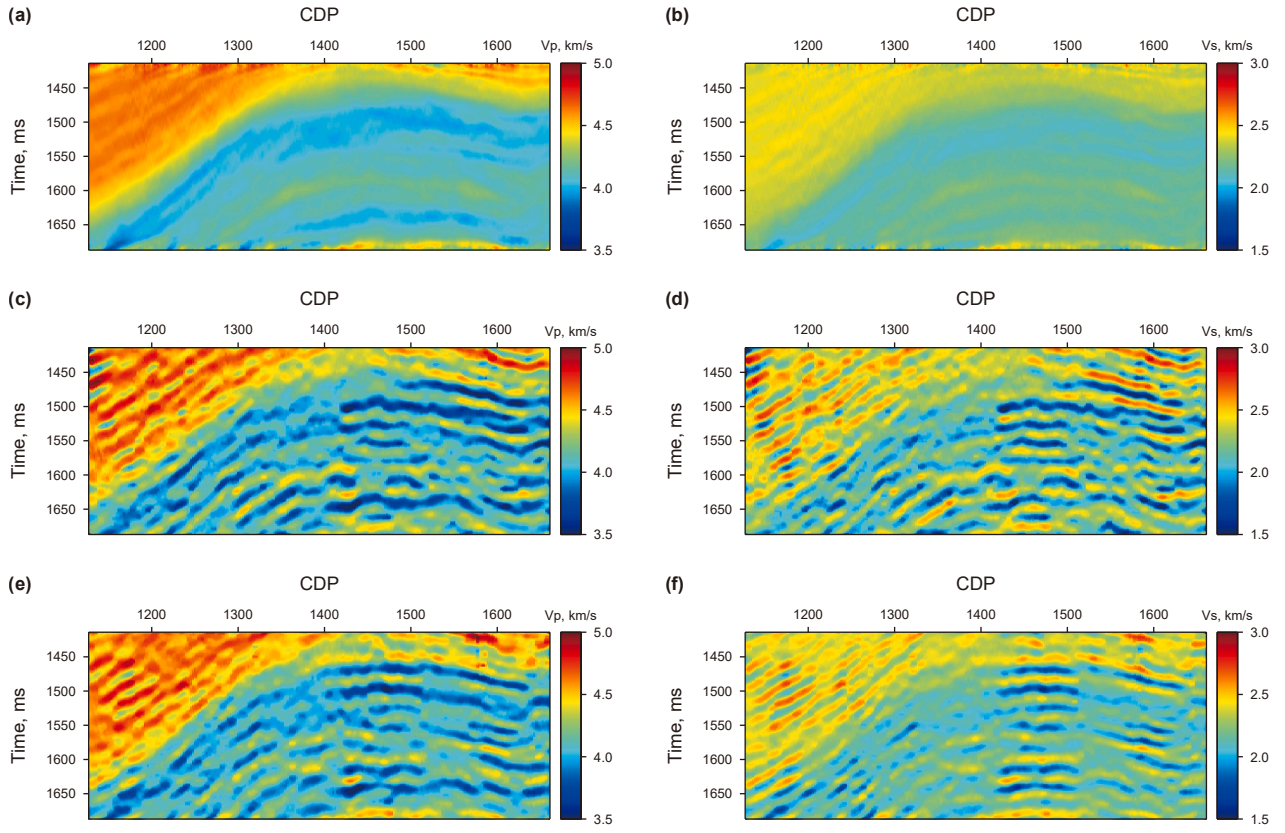

Fig. 11. Panels **(a)** and **(b)** represent the initial P- and S-wave velocity (Vp and Vs) models. Panels **(c)** and **(d)** represent the inverted P- and S-wave velocity models using PP-wave inversion. Panels **(e)** and **(f)** represent the inverted P- and S-wave velocity models using joint PP and PS inversion.

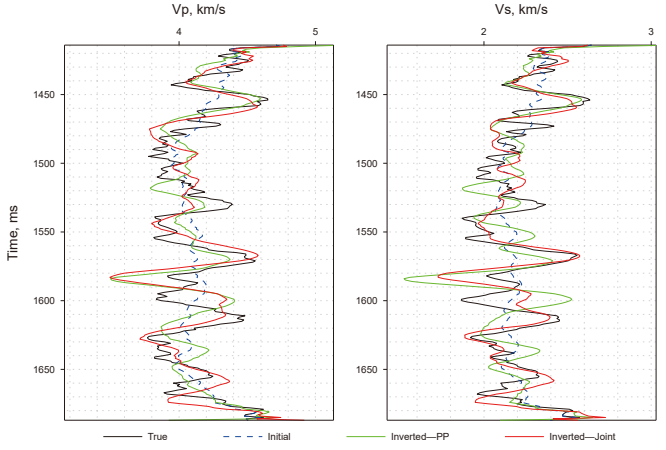

Fig. 12. Inverted P- and S-wave velocity results at the well location (CDP 1396 in Fig. 11). The solid black curves represent the well log data, the dashed blue curves represent the initial model, the green curves represent the inverted values from the PP-wave inversion, and the red curves represent the inverted values from the joint PP and PS inversion. At the well location, the correlation coefficients between the reference and inverted traces improved from 0.56 to 0.67 for P-wave velocity and from 0.39 to 0.70 for S-wave velocity.

the well logs than those of the PP-wave inversion. At the well location, the correlation coe-cients between the reference and inverted traces improved from 0.56 to 0.67 for P-wave velocity and from 0.39 to 0.70 for S-wave velocity.

5. Discussion

In this paper, we used the predicted PS-waves to perform the further conventional joint PP and PS inversion, which is necessary because directly predicting velocity and density using deep learning remains uncertain and unstable. Conventional algorithms, which have been reliably applied to field data for decades, offer more stability and can incorporate various constraints. These algorithms not only invert velocities and densities but also other elastic and rock physics properties, seamlessly integrating with mature software using predicted prestack data. Accurate PP-wave angle gathers field data alone would make joint PP and PS inversion obsolete, but due to noise and inaccuracies in PP-waves, PS-waves serve as a crucial supplementary constraint, enhancing PP inversion. While deep learning shows promise, its results are not yet fully reliable, making it unsafe to rely solely on deep-learning-predicted PS-waves. A safer and more accurate approach is joint inversion using both field PP data and predicted PS data, leveraging the strengths of each. Additionally, predicted PS waves benefit imaging processes, further justifying their prediction and use.

The proposed method is based on the assumption that the amplitude variation with the incident angle in PP-wave angle gathers follows the Zoeppritz equation, which inherently includes the assumptions of AVO/AVA inversion. These assumptions are: 1) only pure P-wave reflections are preserved in PP-wave angle gathers; 2) the strata are uniform; 3) the propagation paths of seismic waves in subsurface media are linear, or the curvature has a negligible impact; and 4) seismic waves propagate as plane

waves. Additionally, this study only considers isotropic media, whereas the real subsurface may be anisotropic and/or viscoelastic. Moreover, during the training of the deep learning model, only random white noise was added, while more complex noise, such as multiples, could exist and cannot be ignored. Furthermore, in this study, we only predict the amplitude or AVA information of PS-waves; the travel time and waveform information are not predicted. An upgraded version may take kinematic information into consideration.

Before performing the joint inversion of PP and PS data, real field PS-wave angle gathers should be provided for comparison with the learned PS. However, well-matched PP- and PS-wave pairs are hard to come by, and field PS-waves often suffer from low signal-to-noise ratios. Despite these challenges, field PS-waves remain valuable and serve as important references. Unfortunately, we don't have such data available for this study. Instead, we adopt a compromise approach: comparing the predicted PS-wave angle gathers from the PP-wave angle gathers at the well location with the synthetic PS angle gathers derived from well log data.

The training data used in this study are synthetic. Training deep learning models with real PS data poses additional challenges, as reliable PP-PS wave pairs are typically available only from a limited number of field locations, making access difficult for most researchers. This lack of datasets diversity hinders the model's ability to generalize across varied geological conditions. Moreover, acquiring high-quality PP and PS wave pairs is often resource-intensive and technically complex. Relying solely on real data for training could significantly slow progress in geophysical applications.

To address inconsistencies between the actual input size and the pretrained model's requirements, we divide the input data into smaller patches that match the model's input size, process each patch individually, and then reconstruct the output by merging the processed patches.

The PS gather predicted using the deep learning method based on the PP gather implies that the PS and PP gathers have nearly identical structural images in thus study. However, in real reservoir prediction, P- and S-waves respond differently to the reservoir (oil or gas), meaning that the PP and PS gathers are not the same. In fact, the structural similarity of the strata is a key feature in seismic data. PP and PS gathers often exhibit similar structural characteristics because they are derived from the same subsurface structure. It is logical that the deep learning model captures this, as in most cases, the propagation paths of seismic waves and the stratigraphy are correlated. Therefore, the structural similarity between the PP and PS gathers is not necessarily a problem. However, P-waves and S-waves often respond differently to reservoirs (such as oil and gas). The reflection characteristics of P- and S-waves, especially in the presence of hydrocarbons, can lead to differences between the PP and PS gathers in certain details. This is because P- and S-waves react differently to the physical properties of rocks (such as elastic moduli, porosity, etc.) and the presence of fluids. In practical applications, while the strata structure is usually similar, to better predict oil and gas, more physical information should be incorporated into the model. For example, combining rock physics models or elastic parameters could improve the differentiated prediction between the PS and PP gathers. This approach can help the model more accurately capture the different responses of P and S-waves to oil and gas reservoirs, rather than focusing solely on their structural similarity. Overall, while the structural similarity of the strata is an important feature, further consideration of the different responses of P and S-waves would be essential for improving the model's accuracy and its ability to predict oil and gas reservoirs.

This paper does not account for wavelet variation with incident angle, which may limit the applicability of the proposed method when such variations are significant. Therefore, when applying this method to predict PS-wave gathers from field PP-wave gathers, appropriate preprocessing should be performed to minimize wavelet differences across angles and enhance the method's robustness. Furthermore, a potential improvement to the proposed approach would be to incorporate angle-dependent wavelet characteristics into the training data. This could allow the trained model to generalize better to a wider range of real field data, although it would likely require a larger training datasets and a more advanced deep learning architecture.

Moreover, although the proposed method demonstrates strong overall performance, subtle discrepancies between the predicted and true results still persist. To further improve accuracy, we suggest exploring alternative deep learning architectures, such as Vision Transformers (ViT), Swin Transformers, or diffusion models, which may provide enhanced feature extraction and generalization in complex settings. In addition, incorporating anisotropy-aware reflection coefficient formulas into the training data generation process could improve the model's adaptability to real-world conditions.

6. Conclusions

We have developed a method utilizing the cGAN deep learning algorithm to predict PS-wave angle gathers from PP-wave angle gathers. Our deep learning model is trained with synthetic data, demonstrating a strong fit between the predicted PS-waves and real PS-waves in a test dataset. Subsequently, the trained deep learning model is applied to actual field PP-waves, maintaining robust performance. The predicted PS-wave angle gather at the well location closely aligns with the synthetic PS-wave angle gather generated using reference well logs. Additionally, the P- and S-wave velocities estimated from the joint PP and PS AVA inversion, based on field PP-waves and the predicted PS-waves, display a superior model fit compared to those obtained solely from the PP-wave AVA inversion using field PP-waves.

CRediT authorship contribution statement

Xin Fu: Writing – original draft, Methodology, Investigation, Conceptualization. **Feng Zhang:** Writing – review & editing, Data curation. **Dan-Ping Cao:** Writing – review & editing, Supervision, Funding acquisition.

Data availability statement

The data that support the finding of this study are available online at https://zenodo.org/records/11172217.

Declaration of competing interest

The authors declare that they have no known competing financial interests or personal relationships that could have appeared to influence the work reported in this paper.

Acknowledgments

This work was funded by the National Natural Science Foundation of China (No. 42325403 and No. 42122029), the Deep Earth Probe and Mineral Resources Exploration - National Science and Technology Major Project (No. 2024ZD1004201), the Young Expert of Taishan Scholars Project (No. tsqn202408095), the Independent

Innovation Research Project (Science and Engineering) - Youth Fund (No. 24CX06012A) of China University of Petroleum, the Qingdao Postdoctoral Funding Program (No. QDBSH20240202023), and the CNPC Investigations on fundamental experiments and advanced theoretical methods in geophysical prospecting applications (2022 DQ0604-02).

References

Aki, K., Richards, P.G., 2002. Quantitative Seismology.

Castagna, J.P., Batzle, M.L., Eastwood, R.L., 1985. Relationships between compressional-wave and shear-wave velocities in clastic silicate rocks. Geophysics 50, 571–581. https://doi.org/10.1190/1.1441933.

Fu, X., 2024. Seismic amplitude inversion based on a new pp-wave reflection coefficient approximation equation for vertical transversely isotropic media. Geophysics 89 (3), R217–R230. https://doi.org/10.1190/geo2023-0132.1.

Fu, X., Zhang, F., Li, X.Y., Yang, S., Ma, G.R., 2018. Simultaneous inversion of P-wave impedance and the ratio of S-to P-wave velocity. In: International Geophysical Conference, Beijing, China, 24-27 April 2018. Society of Exploration Geophysicists and Chinese Petroleum Society, pp. 1193–1196. https://doi.org/10.1190/IGC2018-291.

Fu, X., Cao, D.P., Zhang, F., 2025. Deep learning-based denoising of pre-stack seismic angle gathers with application to time-lapse data. Geophysics 91 (1), 1–82. https://doi.org/10.1190/geo2024-0472.1.

Gardner, G., Gardner, L., Gregory, A., 1974. Formation velocity and density—the diagnostic basics for stratigraphic traps. Geophysics 39 (6), 770–780. https://doi.org/10.1190/1.1440465.

Goodfellow, I., Pouget-Abadie, J., Mirza, M., Xu, B., Warde-Farley, D., Ozair, S., Courville, A., Bengio, Y., 2014. Generative adversarial nets. Adv. Neural Inf. Process. Syst. 27, 2672–2680.

Ioffe, S., Szegedy, C., 2015. Batch normalization: accelerating deep network training by reducing internal covariate shift. In: Proceedings of the 32nd International Conference on International Conference on Machine Learning, pp. 448–456. https://doi.org/10.48550/arXiv.1502.03167.

Isola, P., Zhu, J.Y., Zhou, T., Efros, A.A., 2017. Image-to-image translation with conditional adversarial networks. In: Proceedings of the IEEE Conference on Computer Vision and Pattern Recognition, pp. 1125–1134. https://doi.org/10.48550/arXiv.1611.07004.

Liu, Z.C., Zhang, F., Li, X.Y., 2019. Elastic anisotropy and its influencing factors in organic-rich marine shale of southern China. Sci. China Earth Sci. 62 (11), 1805–1818. https://doi.org/10.1007/s11430-019-9449-7.

Mirza, M., Osindero, S., 2014. Conditional Generative Adversarial Nets. arXiv preprint, arXiv:1411.1784.

Oliveira, D.A., Ferreira, R.S., Silva, R., Brazil, E.V., 2018. Interpolating seismic data with conditional generative adversarial networks. IEEE Geoscience Remote Sensing Letters 15, 1952–1956. https://doi.org/10.1109/LGRS.2018.2866199.

Pathak, D., Krahenbuhl, P., Donahue, J., Darrell, T., Efros, A.A., 2016. Context encoders: feature learning by inpainting. In: Proceedings of the IEEE Conference on Computer Vision and Pattern Recognition, pp. 2536–2544. https://doi.org/10.48550/arXiv.1604.07379.

Radford, A., Metz, L., Chintala, S., 2015. Unsupervised Representation Learning with Deep Convolutional Generative Adversarial Networks. arXiv preprint, arXiv:1511.06434.

Ronneberger, O., Fischer, P., Brox, T., 2015. U-net: convolutional networks for biomedical image segmentation. Medical Image Computing Computer-Assisted Intervention-MICCAI 2015 234–241. https://doi.org/10.1190/1.3555082.

Versteeg, R., 1994. The marmousi experience: velocity model determination on a synthetic complex data set. Lead. Edge 13 (9), 927–936. https://doi.org/10.1190/1.1437051.

Wei, Q., Li, X., Song, M., 2021. Reconstruction of irregular missing seismic data using conditional generative adversarial networks. Geophysics 86 (6), V471–V488. https://doi.org/10.1190/geo2020-0644.1.

Wu, C.Z., Lei, H., Zhang, F., 2023a. Gas hydrate reservoir identification based on rock physics modelling and sensitive elastic parameters. J. Geophys. Eng. 20 (1), 117–127. https://doi.org/10.1093/jge/gxac100.

Wu, C.Z., Zhang, F., Ding, P.B., 2023b. Rock physics model of gas hydrate reservoir with mixed occurrence states. Geophysics 89 (2), 1–57. https://doi.org/10.1190/geo2023-0211.1.

Yang, F., Ma, J., 2019. Deep-learning inversion: a next-generation seismic velocity model building method. Geophysics 84 (4), R583–R599. https://doi.org/10.1190/geo2018-0249.1.

Zhang, F., Zhang, T., Li, X.Y., 2019. Seismic amplitude inversion for the transversely isotropic media with vertical axis of symmetry. Geophys. Prospect. 67 (9), 2368–2385. https://doi.org/10.1111/1365-2478.12842.

Zhang, Z., Wu, Y., Zhou, Z., Lin, Y., 2019. Velocitygan: subsurface velocity image estimation using conditional adversarial networks. In: 2019 IEEE Winter Conference on Applications of Computer Vision (WACV), pp. 705–714. https://doi.org/10.1109/WACV.2019.00080.

Zoeppritz, K., 1919. Erdbebenwellen viii b, uber reflexion und durchgang seismischer wellen durch unstetigkeisflachen. Gottinger Nachr 1, 66–84 (in German).